



Experimental observation of a quadrupolar phase via quench dynamics on a spin simulatorDafa Zhao ^{1,2,3} Shunzhong Xue ^{1,2,3} Dong Ruan,¹ Jun Li,^{2,3} Dawei Lu,^{2,3} Wen Huang,^{2,3} Tao Xin,^{2,3} Hang Li,^{4,*} Xinfang Nie,^{2,3,†} and Guilu Long^{1,4,5,6}¹State Key Laboratory of Low-Dimensional Quantum Physics and Department of Physics, Tsinghua University, Beijing 100084, China²Shenzhen Institute for Quantum Science and Engineering and Department of Physics, Southern University of Science and Technology, Shenzhen 518055, China³Guangdong Provincial Key Laboratory of Quantum Science and Engineering, Southern University of Science and Technology, Shenzhen 518055, China⁴Beijing Academy of Quantum Information Sciences, Beijing 100193, China⁵Frontier Science Center for Quantum Information, Beijing 100084, China⁶Beijing National Research Center for Information Science and Technology, Beijing 100084, China

(Received 8 August 2021; revised 28 September 2021; accepted 14 December 2021; published 29 December 2021)

Recently, higher-order topological insulators have drawn much attention from researchers. For chiral-symmetric one-dimensional systems, the mean chiral displacement, a bulk observable related to the topological invariant, can distinguish topological states from trivial phases. Naturally, there exists an analogous quality for the higher-order one. In a previous work [T. Mizoguchi, Y. Kuno, and Y. Hatsugai, *Phys. Rev. Lett.* **126**, 016802 (2021)], the mean chiral quadrupole moment is introduced. Inspired by this work, we investigate the quadrupolar phase of a higher-order topological insulator on a spin quantum simulator. With focus on a two-particle noninteracting Benalcazar-Bernevig-Hughes model, by changing the amplitude of hopping interactions, we first observe quantum phase transitions from topological phase to trivial phase using a spin simulator experimentally. Since the mean chiral quadrupole moment has robustness against environmental noise, we also test its dependence on perturbations. As an exploration of the bulk observable of a higher-order topological insulator, it may provide one path to investigate arbitrary dimensional systems.

DOI: [10.1103/PhysRevA.104.062615](https://doi.org/10.1103/PhysRevA.104.062615)**I. INTRODUCTION**

In the last century, Ginzburg-Landau theory has dominated people's perception of phase transition [1]. Before the proposal of the two-dimensional Berezinskii-Kosterlitz-Thouless transition [2] and the discovery of the integer or fractional quantum Hall effect [3,4], people had gradually realized that there exist states of matter beyond Landau's phase transition theory [5,6]. These are known as topological states of materials, which can be described by topological invariants (TIs). Most TIs in physics arise as integrals of some geometric quantity and only take on integer values [7]. This means that as long as the geometry of the manifold does not undergo sudden changes, such as the number of holes, the TIs will not change. In topological materials, bulk-boundary correspondence (BBC) is one of the most notable features. For a d -dimensional topological insulator, it has $(d - 1)$ -dimensional gapless edge states. It allows one to predict the edge state of a system based on the knowledge of a bulk topological invariant. Taking the two-dimensional quantum Hall effect as an example [8], a series of integer platforms has been observed experimentally. This is due to the edge states localized at the tails of one-dimensional (1D) states.

However, TIs cannot be directly observed from gapped ground states. According to BBC, they can be detected via characteristic wave functions of edge states. There are many different methods to investigate the topological properties of wave functions. One direct method is to investigate the wave function at every fixed moment [9,10], e.g., the Chern number will preserve it in the Chern insulator after quench. Another way is to investigate band-inversion surfaces in the Brillouin zone. Liu and coworkers [11,12] noticed that when the initial state is in the topological trivial phase the topological properties of the evolution Hamiltonian can be detected via winding number of band-inversion surfaces, and by considering $(d + 1)$ space-time properties of wave functions, such as measuring dynamical Chern number [13], Hopf links [14,15], and mean chiral displacement (MCD) [16,17], TIs can be revealed from time-dependent quantities. For a chiral-symmetric 1D system, the MCD, which is the polarization weighted by the eigenvalue of the chiral operator, was introduced to characterize winding number in the Su-Schrieffer-Heeger (SSH) model [18,19]. More precisely, it can dictate the winding number of 1D TIs in AIII and BDI classes [20]. Analogously, Mizoguchi *et al.* [21] proposed that this method can be extended to higher-order systems by introducing the mean chiral quadrupole moment (MCQM), the long-time average of which can also characterize the topology.

Thanks to progress in quantum simulators, experimentally detecting TIs is accessible in various kinds of platforms, e.g.,

*lihang@baqis.ac.cn

†niexf@sustech.edu.cn

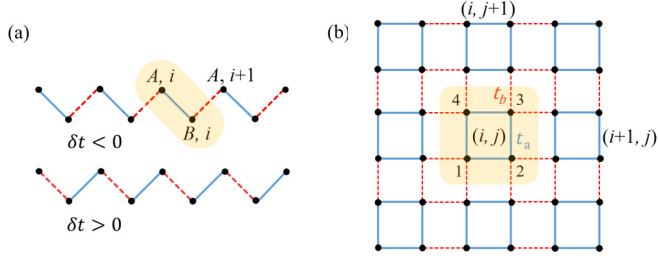


FIG. 1. Schematic of (a) the SSH model and (b) the BBH model. (a) The solid and dashed lines represent the long and short bonds of hopping. When $\delta t < 0$ or $\delta t > 0$, it corresponds to two distinct phases in the SSH model. (b) The sites on a square lattice specified by the position label of the unit cell $\mathbf{r} = (i, j)$ or (r_x, r_y) and the site label $\alpha = 1, 2, 3, 4$. Solid blue and dashed red lines stand for the intracellular and intercellular hoppings, respectively.

ultracold atoms [22–24], superconductors [25,26], twisted photons [27], disordered atomic wires [28], and nuclear magnetic resonance (NMR) [29]. The MCD has already been widely used in characterizations of the SSH model and extended SSH models [16,17,27,30]. Yet, the MCQM has merely stayed at the primary theoretical stage so far. As the NMR system has many merits, such as long coherent time and precise control, it can be regarded as an ideal quantum simulator [31–35] to observe the MCQM experimentally. Hereafter, we report an experimental observation of the quadrupolar phase based on the NMR spin simulator.

In this article, we mainly focus on one typical two-dimensional higher-order topological insulator. First, we experimentally observe the MCQM oscillations under different intercell and intracell hopping amplitudes. Then we utilize the MCQM to characterize the phase transition of the bulk via quench dynamics. Additionally, the feature of noise dependence is also explored in our experiments. This article is organized as follows. In Secs. II and III, warming up from the one-dimensional chiral topological SSH model, the two-dimensional Benalcazar-Bernevig-Hughes (BBH) model [36,37] is introduced briefly, which is one type of higher-order topological insulator with a quantized electric multipole. In Sec. IV, we show how our experiments are designed and present the experimental results. Finally, the conclusion and discussion related to this paper are given in Sec. VI.

II. THE MCD IN THE SSH MODEL

The SSH model describes spinless electrons hopping in a polyacetylene chain (one-dimensional lattice), with staggered hopping amplitudes.

As shown in Fig. 1(a), the SSH model can be simply described by a single-particle Hamiltonian, of the form

$$\mathcal{H}_{\text{SSH}} = \sum_{n=1}^N (t + \delta t) c_{A,n}^\dagger c_{B,n} + \sum_{n=1}^{N-1} (t - \delta t) c_{A,n+1}^\dagger c_{B,n} + \text{H.c.}, \quad (1)$$

where $c_{A(B),n}^\dagger$ and $c_{A(B),n}$ are the creation and annihilation operators of the electron on the n th site of A (or B), respectively. In this model, each unit cell consists of two sites. The hopping

amplitude in the unit cell is $t + \delta t$ and that between two unit cells is $t - \delta t$.

The SSH model indicates that the polyacetylene actually has two distinct topological phases. Assuming that $t > 0$, it is topologically trivial for $\delta t > 0$, but nontrivial for $\delta t < 0$, which means a topological quantum transition occurs at $\delta t = 0$. The MCD [16,17], defined as

$$\mathcal{C}_d(t) = \sum_i \langle \psi_i(t) | \hat{\Gamma} \hat{P} | \psi_i(t) \rangle, \quad (2)$$

is introduced to characterize these two phases, where $\hat{\Gamma}$ is a chiral operator satisfying $\hat{\Gamma}^2 = 1$ and anticommutes with Hamiltonian \mathcal{H} ($\hat{\Gamma} \mathcal{H} = -\mathcal{H} \hat{\Gamma}$). \hat{P} is the position operator, acting as $\hat{P}|x\rangle = x|x\rangle$.

As one typical chiral system, the SSH model can be characterized by topological invariants, such as the Berry phase, the Chern number, the nested Wilson loop, and entanglement-related quantities. In previous work [30], it was found that in the long-time limit $\mathcal{C}_d(t \rightarrow \infty) \rightarrow \nu$, where $\nu = \text{Tr}[\Gamma H^{-1} \partial_q H]$ is the winding number of the chiral Hamiltonian $H(q)$ generating the dynamics after the quench defined in the quasimomentum space. Therefore, the MCD of a single particle can be regarded as a topological marker in experiments between different topological phases.

III. THE MCQM IN THE BBH MODEL

As an extension of the theory of dipole moments in crystalline insulators to higher multipole moments, Benalcazar, Bernevig, and Hughes proposed the concept of quantized electric multipole insulators [36,37], of which the dipole moment is zero but with quantized quadrupole moment. The Hamiltonian of the BBH model is given as follows:

$$\mathcal{H}_{\text{BBH}} = \sum_{(i,j)} \{ [t_x + (-1)^i \delta t_x] c_{i+1,j}^\dagger c_{i,j} + [t_y + (-1)^j \delta t_y] c_{i,j+1}^\dagger c_{i,j} \} + \text{H.c.}, \quad (3)$$

where $c_{i,j}^\dagger$ and $c_{i,j}$ denote the creation and annihilation operators of spinless fermions on the site (i, j) . t_x and t_y are the transfer integrals between the nearest-neighbor pairs of sites as shown in Fig. 1(b). There are two types of hopping in the x and y direction such as $t_x \pm \delta t_x$ and $t_y \pm \delta t_y$, which correspond to intercellular and intracellular hoppings, respectively.

The topological nature of the Hamiltonian \mathcal{H}_{BBH} has been well investigated in the literature. For simplicity, we set $t_x = t_y = t$, $\delta t_x = \delta t_y = \delta t$ and define $t_a = t - \delta t$ and $t_b = t + \delta t$. When $|t_a| \neq |t_b|$, the system is gapped at half filling. The half-filled ground state is topologically trivial (nontrivial) when $|t_a| > |t_b|$ ($|t_a| < |t_b|$). In order to capture the properties of the topological phase in the BBH model quantitatively, the MCQM is introduced as

$$\mathcal{C}_q(t) = \langle \Psi(t) | \mathcal{Q} | \Psi(t) \rangle, \quad (4)$$

wherein $\mathcal{Q} = \sum_{\mathbf{r}, \alpha} r_x r_y \hat{\Gamma}_\alpha n_{\mathbf{r}, \alpha}$ is the quadrupole operator, a pair of indices $\mathbf{r} = (r_x, r_y)$ is the position of the unit cell, and $\Psi(t)$ is the wave function after quench dynamics. The site-resolved particle density is defined as $n_i = c_i^\dagger c_i$, which is all we need to measure in actual experiments.

Analogously, $\hat{\Gamma}_\alpha$ is the eigenvalue of the chiral operator, a factor similar to $\hat{\Gamma}$ in the MCD heuristically. It takes $+1$ for $\alpha = 1, 3$ and -1 for $\alpha = 2, 4$, which makes the contributions from the negative-energy bands and those from the positive-energy band additive, otherwise they may cancel each other. In one special case, for the two-particle BBH model [21], $\bar{C}_q = 0$ indicates the trivial phase, and $\bar{C}_q = 1/2$ indicates the topological phase, where \bar{C}_q stands for the long-time average of $C_q(t)$.

In a nutshell, the MCQM can be regarded as an extension of the MCD to characterize the two-dimensional second-order topological insulator. To make the MCQM well defined, the unit cells and sublattices need to be fixed at the beginning, since it depends on the the choice of the frame.

IV. EXPERIMENTAL DESIGN

This model consists of four degrees of freedom, two for sites and the other two for cells. Since each qubit is equivalent to a two level system, i.e., one degree of freedom, these four degrees of freedom can be encoded into a four-qubit quantum simulator, ^{13}C -iodotrifluoroethylene ($\text{C}_2\text{F}_3\text{I}$) dissolved in d -chloroform [38–44], as shown in Fig. 2(a).

It has one ^{13}C nucleus and three ^{19}F nuclei as four qubits. The four unit cells $\mathbf{c} = \{\text{I, II, III, IV}\}$ are encoded into the subspace of the F_2 and F_3 qubits. In each sublattice cell, there are four sites $\mathbf{s} = \{1, 2, 3, 4\}$ encoded with the ^{13}C and F_1 qubits. According to this coding rule, each particle has its own position coordinate (\mathbf{c}, \mathbf{s}) .

We investigate the two-particle BBH model of 4×4 unit cells on the Bruker Ascend 600-MHz spectrometer (14.1 T) equipped with a cryoprobe (20-K helium gas) at room temperature (298 K). Under the condition of weak-coupling approximation, the internal Hamiltonian of the NMR system is given as

$$\mathcal{H}_{\text{NMR}} = - \sum_{i=1}^4 \omega_i I_i^z + \sum_{i=1, i < j}^4 2\pi J_{ij} I_i^z I_j^z, \quad (5)$$

where $\omega_i/2\pi$ is the Larmor frequency of the i th spin; I_i^z and I_j^z are the z -direction spin bases of the i th and j th nucleus, respectively; and J_{ij} is the scalar coupling between them. More chemical property details about the $\text{C}_2\text{F}_3\text{I}$ molecule are given in Fig. 2(b).

Naturally, the nuclei are governed by the Boltzmann distribution, which cannot be observed directly. We use the line selection technique to drive thermal equilibrium state $\rho_{\text{eq}} = \mathcal{I}^{\otimes 4}/16 + \epsilon(\gamma_{\text{C}} I_1^z + \gamma_{\text{F}} I_2^z + \gamma_{\text{F}} I_3^z + \gamma_{\text{F}} I_4^z)$ into the pseudopure state (PPS) [31,45–47]

$$\rho_{\text{PPS}} = \frac{1 - \epsilon}{16} \mathcal{I}^{\otimes 4} + \epsilon |0000\rangle\langle 0000|, \quad (6)$$

where $\mathcal{I}^{\otimes 4}$ stands for the tensor product of four 2×2 identity operators, the polarization $\epsilon \approx 10^{-5}$, and γ_{C} (γ_{F}) is the gyromagnetic ratios of the ^{13}C (^{19}F) nuclei. The first term of Eq. (6) is always neglected [48], since it has no contribution to the experimental signal. The second term evolves under an rf field following the Hamiltonian propagator.

The quench dynamics [49,50] can be extracted by the unitary time evolution of the many-body wave function under the

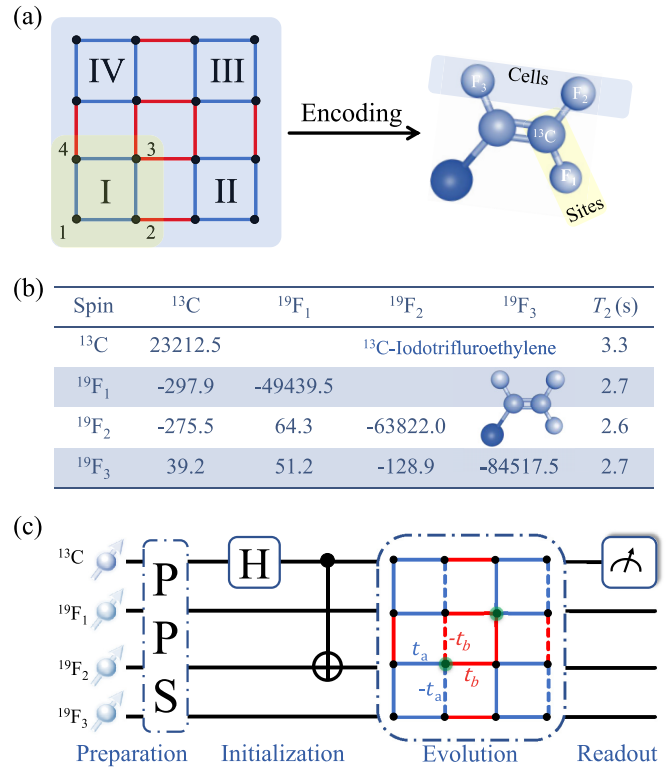


FIG. 2. Experimental design and characteristics of the $\text{C}_2\text{F}_3\text{I}$ molecule. (a) The four-qubit quantum simulator is divided into two subspaces, encoding the cells {I, II, III, IV} and the sites {1,2,3,4} in the two-particle BBH model. (b) The molecule chemical parameters of ^{13}C -iodotrifluoroethylene dissolved in d -chloroform. The table lists the chemical shifts (diagonal, in hertz) and J couplings (off-diagonal, in hertz), respectively. Relaxation time T_2 (in seconds) is also listed in the last column. (c) Quantum circuit to realize the observation of the quadrupolar phase in the BBH system. In the *Evolution* module, the initial positions of the two particles are represented by green circles. The diagram in the dash-dotted line box shows the construction of the quench Hamiltonian \mathcal{H}_q . The solid (dashed) bonds stand for t_a/t_b ($-t_a/-t_b$) of the hopping amplitude.

quench Hamiltonian \mathcal{H}_q :

$$|\Psi(t)\rangle = e^{-i\mathcal{H}_q t} |\Psi_0\rangle. \quad (7)$$

Herein, we set $\hbar = 1$. As shown in Fig. 2(c), the opposite corners at the center of the system are occupied by two particles initially, with position coordinates (I, 3) and (III, 1). According to our encoding rule, the initial state of these two particles happens to be the Bell state in the subspace of first (^{13}C) and third ($^{19}\text{F}_2$) qubits:

$$|\Psi_0\rangle = |0_2 0_4\rangle \otimes (|0_1 1_3\rangle + |1_1 0_3\rangle). \quad (8)$$

The initial state can be generated by the composition of Hadamard and controlled-NOT (CNOT) gates.

As our objective is to demonstrate the feasibility of detecting the higher-order topology on our NMR simulator, we hereby focus exclusively on noninteracting models for simplicity, leaving the effect of interactions for future study. The quench Hamiltonian \mathcal{H}_q of the noninteracting two-particle BBH model with which we are concerned is depicted in the *Evolution* module of Fig. 2(c). It includes three commu-

tative terms, intracell part \mathcal{H}_a , intercell part \mathcal{H}_b , and disorder part \mathcal{H}_w , as follows:

$$\mathcal{H}_q = \mathcal{H}_a + \mathcal{H}_b + \mathcal{H}_w, \quad (9)$$

where

$$\mathcal{H}_a = t_a \sum_{\mathbf{c}} (c_{\mathbf{c},1}^\dagger c_{\mathbf{c},2} + c_{\mathbf{c},3}^\dagger c_{\mathbf{c},4} + c_{\mathbf{c},1}^\dagger c_{\mathbf{c},4} - c_{\mathbf{c},2}^\dagger c_{\mathbf{c},3}) + \text{H.c.}, \quad (10)$$

$$\begin{aligned} \mathcal{H}_b = t_b \sum_{\mathbf{c}} & (c_{\mathbf{c}+\mathbf{e}_x,1}^\dagger c_{\mathbf{c},2} + c_{\mathbf{c}+\mathbf{e}_x,3}^\dagger c_{\mathbf{c},4} \\ & + c_{\mathbf{c}}^\dagger c_{\mathbf{c}+\mathbf{e}_y,1} c_{\mathbf{c},4} - c_{\mathbf{c}+\mathbf{e}_y,2}^\dagger c_{\mathbf{c},3}) + \text{H.c.}, \end{aligned} \quad (11)$$

and

$$\mathcal{H}_w = \sum_{i \in \{\mathbf{c}, \mathbf{s}\}} w_i c_i^\dagger c_i. \quad (12)$$

We set the length of the sublattice cells to be unity, and \mathbf{e}_x and \mathbf{e}_y are unit vectors in x and y directions, respectively. With the dynamical process, the two particles hop randomly in the nearest-neighbor sites, and t_a ($-t_a$) and t_b ($-t_b$) are

the strength of intracell and intercell hopping amplitudes. The summation index (\mathbf{c}, \mathbf{s}) in Eqs. (10) and (11) is under the open boundary condition. For the I and IV cells, $\mathbf{c} + \mathbf{e}_x$ means the II and III cells. In the same vein, for the I and II cells, $\mathbf{c} + \mathbf{e}_y$ means the III and IV cells. In Eq. (12), coefficient w_i is the strength of i th site disorder potential chosen randomly within the amplitude of $[-w, w]$.

In order to implement the quench dynamics of \mathcal{H}_q on a spin quantum simulator, we employ the Jordan-Wigner transformation to map this fermionic system into a collection of qubits. It is a natural way in that a given fermionic mode with or without occupied states is just analogous to a spin qubit with two possible states $\{|0\rangle, |1\rangle\}$. For spinless fermions, the fermionic creation operator corresponds to a string of Pauli operators $c_j^\dagger = \sigma_j^\dagger \otimes_{i=1}^{j-1} \sigma_i^z$ and the fermionic annihilation operator $c_j = (c_j^\dagger)^\dagger$, where the Pauli creation and annihilation operators $\sigma_\pm = (\sigma^x \pm i\sigma^y)/2$ and σ_j^α ($\alpha = x, y, z$) are the Pauli matrices. The anticommutation relations $\{c_{j,s}, c_{l,s}^\dagger\} = \delta_{j,l} \delta_{s,s'}$, $\{c_{j,s}^\dagger, c_{l,s'}^\dagger\} = \{c_{j,s}, c_{l,s'}\} = 0$, $c_j^\dagger c_{j+1} = \sigma_j^\dagger \sigma_{j+1}^-$, and $c_j^\dagger c_j = \sigma_j^\dagger \sigma_j^- = (\mathcal{I} + \sigma_j^z)/2$ are easily satisfied. After this transformation, the quench Hamiltonian \mathcal{H}_q of Eq. (9) can be rewritten as

$$\begin{aligned} \mathcal{H}_q = \sum_{\mathbf{c}} & t_a (\sigma_{\mathbf{c},1}^\dagger \sigma_{\mathbf{c},2} + \sigma_{\mathbf{c},3}^\dagger \sigma_{\mathbf{c},4} + \sigma_{\mathbf{c},1}^\dagger \sigma_{\mathbf{c},4} - \sigma_{\mathbf{c},2}^\dagger \sigma_{\mathbf{c},3}) + \text{H.c.} \\ & + \sum_{\mathbf{c}} t_b (\sigma_{\mathbf{c}+\mathbf{e}_x,1}^\dagger \sigma_{\mathbf{c},2} + \sigma_{\mathbf{c}+\mathbf{e}_x,3}^\dagger \sigma_{\mathbf{c},4} + c_{\mathbf{c}}^\dagger \sigma_{\mathbf{c}+\mathbf{e}_y,1} \sigma_{\mathbf{c},4} - \sigma_{\mathbf{c}+\mathbf{e}_y,2}^\dagger \sigma_{\mathbf{c},3}) + \text{H.c.} + \sum_{i \in \{\mathbf{c}, \mathbf{s}\}} w_i (\mathcal{I} + \sigma_i^z)/2, \end{aligned} \quad (13)$$

which is directly used to realize the evolution process.

The original plain idea is to decompose the evolution process $U_q = e^{-i\mathcal{H}_q t}$ into single-qubit rotations $R_{x,y,z}(\phi)$ and multiqubit controlled rotations, e.g., the CNOT gate. However, because of the complexity of \mathcal{H}_q , we turn to realize the dynamical process by shaped rf pulse sequences, which are optimized by the gradient ascent pulse engineering (GRAPE) algorithm [51,52]. The rf control Hamiltonian of the four-qubit NMR simulator is

$$\mathcal{H}_{\text{con}} = B_x^C \sigma_x^1 + B_y^C \sigma_y^1 + \sum_{k=2}^4 (B_x^F \sigma_x^k + B_y^F \sigma_y^k), \quad (14)$$

where pairs of $\{B_{x,y}^C, B_{x,y}^F\}$ are the parameters to be optimized in the gradient-based search process. In our experiment, the whole dynamical process is implemented with 1500 slices of a 20- μs square wave pulse, and each slice acts as a unitary operator $U_i(t) = e^{-i(\mathcal{H}_q + \mathcal{H}_{\text{con}})t}$. The fidelity of the optimized pulse is over the average of 0.995, concerning the imperfection of the pulse sequence.

Although the $\text{C}_2\text{F}_3\text{I}$ molecule provides four qubits as a quantum simulator, only the first qubit in the carbon channel is friendly for readout. Fortunately, the first qubit (^{13}C) holds enough information to calculate the MCQM. At the end of dynamical evolution, the bulk topology of the quadrupolar phase can be extracted from the expectation value of $\langle \sigma_z^C \rangle$ of the first qubit. More details related to the measurement process are given in the Appendix.

V. RESULTS AND DISCUSSION

We assume the system is clean without any disorder potentials, only taking hopping terms into consideration. First, we study the MCQM of the two-particle model of different sizes of cells, with the numerical results shown in Fig. 3(a). The ratio $|t_a|/|t_b|$ is changed incrementally by step 0.1 within the range of [0,3]. The total evolution time of every quench dynamical process is 100 s, and we record the evolution by every 0.1 s, then average $C_q(t)$ to get long period mean value $\bar{C}_q = \lim_{T \rightarrow \infty} (1/T) C_q(t) dt$. It was found that, with size of cells increasing, the slope of \bar{C}_q at the transition point becomes sharper than with the smaller size and the critical point tends to be 1.

Experimentally, with the change of the ratio of hopping amplitudes $|t_a|/|t_b|$ in a sequence of the second-order arithmetic progression [0, 0.1, 0.3, 0.6, 1.0, 1.5, 2.1, 2.7], the MCQM oscillates differently. We exhibit three different oscillation behaviors in Figs. 3(b)–3(d), corresponding to $|t_a|/|t_b|$ of the value 0.1, 1.0, and 2.1. The total evolution time is 30 s with a step size of 0.1 s. Based on these experimental results, it is easy to obtain the long period average \bar{C}_q as sketched in Fig. 3(e). Just like the prediction from the theoretical work, we have observed the system gradually goes through the topological phase into the trivial phase. In the topological phase ($|t_a|/|t_b|=0.1$), $C_q(t)$ performs standard cosinusoidal oscillation and \bar{C}_q is 0.50 ± 0.01 . Conversely, in the trivial phase ($|t_a|/|t_b|=2.1$), $C_q(t)$ displays irregular periodic

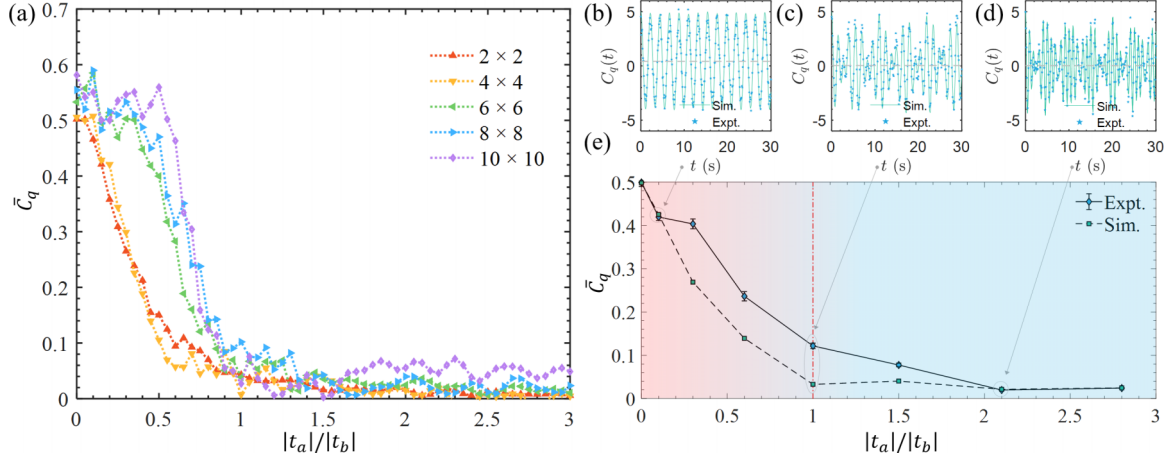


FIG. 3. Theoretical and experimental results of the MCQM in different parameters. (a) Numerical study of the topological phase transition in different sizes of 2×2 , 4×4 , 6×6 , 8×8 , and 10×10 cells. Experimental oscillation behaviors in different cases of (b) Topological phase ($|t_a|/|t_b|=0.1$). (c) Critical point ($|t_a|/|t_b|=1.0$). (d) Trivial Phase ($|t_a|/|t_b|=2.1$). The grey dashed lines are the value of \bar{C}_q . (e) The experimental time-averaged \bar{C}_q as a function against the ratio of hopping amplitude $|t_a|/|t_b|$. Setting $t_b = 1.0$, the value of t_a is varied following the second-order arithmetic progression 0, 0.1, 0.3, 0.6, 1.0, 1.5, 2.1, 2.7.

oscillations violently where \bar{C}_q is 0.02 ± 0.00 approaching to zero.

We also found that the experimental results perform a little deviation from theoretical prediction when $|t_a|/|t_b|$ is in the transition interval, and each data point has a relatively larger error bar. The deviation accumulates from the systemic and accidental errors. It is inevitable that the precision of the NMR spectrometer is limited to instrument noise from internal electronics and instability of the environment. More importantly, the *Initialization* and *Evolution* modules are realized by 1500 slices of a $20\text{-}\mu\text{s}$ shaped square pulse sequence optimized by the GRAPE technique with the fidelity of 0.995, and the total duration time τ is up to 0.3 s. Roughly taking the decoherence effect into consideration, the dynamics evolution of the i th slice can be written as $\rho(t_{i+1}) = \epsilon U_i^\dagger \rho(t_i) U_i$. For each qubit, the Kraus representation of the decoherence channel can be described as $\epsilon(\rho) = E_0 \rho E_0^\dagger + E_1 \rho E_1^\dagger$, where $E_0 = \sqrt{\gamma} \mathcal{I}$, $E_1 = \sqrt{1-\gamma} \sigma_z$ with the parameters $\gamma = [1 + \exp(-\tau/T_2^*)]/2$. In addition, the measurement errors also make a few contributions to the deviation, including the instrument resolution and imperfection readout pulse. It is worth mentioning that in the absolute topological or trivial phase region the effect of noise is not significant, which indicates that the MCQM is an ideal indicator to reveal phase transition against experimental perturbations. Overall, experimental accuracy based on cosine similarity defined as $(\mathbf{a} \cdot \mathbf{b})/(|\mathbf{a}| \cdot |\mathbf{b}|)$ is about 97.59%, conforming to theoretical expectations.

Furthermore, the phase transition indicated by \bar{C}_q is pretty smooth as expected, rather than a steep jump around the critical point $|t_a|/|t_b| = 1.0$. On the one hand, it is due to the limited size of 2×2 cells. On the other hand, it is a typical property of dynamical states [21]. Since ground states are usually characterized by the jump of the quantized topological number, there exists a sharp jump when it goes through different phases. These dynamical properties can be utilized to discriminate the dynamical states from the ground states.

Moreover, we inject the Gaussian noise [53–55] with strength w into the Hamiltonian \mathcal{H}_q of the noninteracting two-particle BBH model ($t_a = -0.3$, $t_b = -1.0$) to study disorder potential dependence properties of the MCQM. The noise is generated randomly obeying the Gaussian distribution of $N(\mu, \sigma) \sim N(0, w)$. We repeat the dynamical oscillation process with the same noisy strength for five turns as a group to observe behaviors of the MCQM in different noise strengths. As shown in Fig. 4, for weak ($w = 0.2$), moderate ($w = 0.6$), and strong ($w = 1.0$) strength cases, the oscillations of $C_q(t)$ behave similarly in the short-time range within 10 s. It is easy to understand that the particles do not reach the boundary in a short time. However, when evolution time t is over 10 s, it oscillates differently as the boundary effect contributes more disorder. With the increasing of noise strength, the average

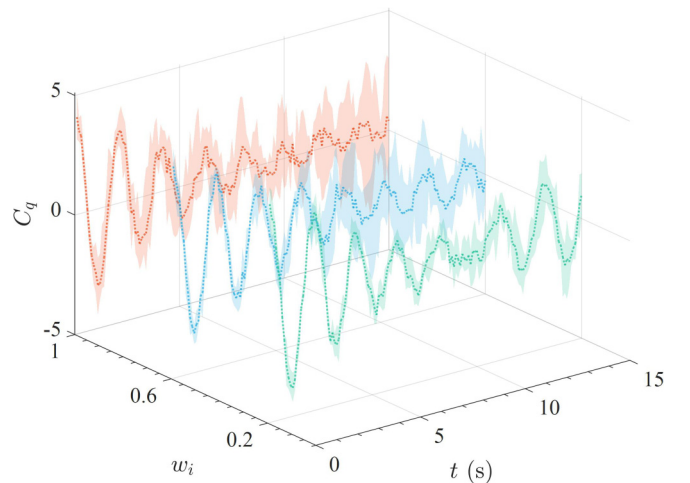


FIG. 4. The dynamical behaviors of the MCQM in weak ($w = 0.2$), moderate ($w = 0.6$), and strong ($w = 1.0$) noise strength. Dashed lines are the average MCQM in five turns of experiments, and the shaded area is the distribution interval correspondingly

\bar{C}_q deviates from the theoretical value 0.4171 obviously. The $C_q(t)$ for the weak strength noise has a slim appearance. But for the strong noise case, it appears bloated, which means it has a greater uncertainty.

These results show that the MCQM can be an experimental indicator of the bulk topology when the noise is within reasonable strength range. Even in the case of strong noise, it is still effective in a short period of time. And for a larger BBH system, the effective period range may be extended reasonably.

VI. CONCLUSION

In conclusion, we utilize the mean chiral quadrupolar moment to study the topology of chiral two-dimensional systems, showing the useful techniques of quantum simulators. We first observe the MCQM on a spin simulator and record its phase transition via quench dynamics. We also test its noise-dependent characters, verifying its robustness against moderate noise. The idea Mizoguchi *et al.* [21] proposed is verified experimentally. Meanwhile, we propose the idea of applying the MCQM onto other platforms. With regard to the experimental characterization of the MCQM in bosonic or anyonic systems, it is also an intriguing topic for future study. What is more, we may pave the way to extend similar ideas to arbitrary dimensional topological systems [56].

Note added. Recently, we found one relevant work [57] based on superconducting circuits to study the BBH model.

ACKNOWLEDGMENTS

D.Z., S.X., D.R., and G.L. are supported by the National Key Research and Development Program of China (Grant No. 2017YFA0303700), the Key Research and Development Program of Guangdong province (Grant No. 2018B030325002), Beijing Advanced Innovation Center for Future Chip, and the National Natural Science Foundation of China (Grant No. 11774197). We are grateful to Dr. S. Wei for helpful discussions. X.N., T.X., J.L., and D.L. are supported by the National Key Research and Development Program of China (Grant No. 2019YFA0308100); the National Natural Science Foundation of China (Grants No. 11975117, No. 11875159, No. 11905099, and No. U1801661); Science, Technology, and Innovation Commission of Shenzhen Municipality (Grant No. JCYJ20180302174036418); Guangdong Basic and Applied Basic Research Foundation (Grant No. 2019A1515011383); and Guangdong Provincial Key Laboratory (Grant No. 2019B121203002).

D.Z. and S.X. contributed equally to this work.

APPENDIX: TRANSLATION OF $\langle \sigma_z^C \rangle$ INTO THE MCQM

In our four-qubit quantum simulator, the wave function can be written as $|\Psi\rangle = [a_1, a_2, \dots, a_{16}]^\dagger$, $a_i \in [0, 1]$, which means the probability of existence at each site. Thus a density matrix of 16×16 dimension correspondingly is shown as

below:

$$\rho = \begin{bmatrix} a_1^* a_1 & a_1^* a_2 & \cdots & a_1^* a_{16} \\ a_2^* a_1 & a_2^* a_2 & \cdots & a_2^* a_{16} \\ \vdots & \vdots & \ddots & \vdots \\ a_{16}^* a_1 & a_{16}^* a_2 & \cdots & a_{16}^* a_{16} \end{bmatrix}_{16 \times 16}. \quad (\text{A1})$$

It follows that $C_q(t) = \langle \Psi(t) | \mathcal{Q} | \Psi(t) \rangle$, where the quadrupolar is

$$\begin{aligned} \mathcal{Q} = & \sum_{r,\alpha} r_x r_y \hat{\Gamma}_\alpha n_{r,\alpha} = r_x r_y (n_{\text{I},1} - n_{\text{I},2} + n_{\text{I},3} - n_{\text{I},4}) \\ & + r_{x+1} r_y (n_{\text{II},1} - n_{\text{II},2} + n_{\text{II},3} - n_{\text{II},4}) \\ & + r_x r_{y+1} (n_{\text{III},1} - n_{\text{III},2} + n_{\text{III},3} - n_{\text{III},4}) \\ & + r_{x+1} r_{y+1} (n_{\text{IV},1} - n_{\text{IV},2} + n_{\text{IV},3} - n_{\text{IV},4}). \end{aligned} \quad (\text{A2})$$

The value of $\mathbf{r} = (r_x, r_y)$ will influence the amplitude of dynamical oscillation behaviors of the MCQM. However, it does not change the long-time average \bar{C}_q . Without loss of generality, we set $\mathbf{r} = (r_x, r_y) = (1, 1)$, and the cells $\{\text{I}, \text{II}, \text{III}, \text{IV}\} = \{(1,1), (1,2), (2,1), (2,2)\}$. Notice here we have just the coordinates of the unit cells, but nothing with our coding rules. The measurement operator of the readout process is

$$\begin{aligned} \hat{P} = & \sigma_z \otimes I_2 \otimes I_2 \otimes I_2 \\ = & (|0\rangle\langle 0| - |1\rangle\langle 1|) \otimes (|0\rangle\langle 0| + |1\rangle\langle 1|)^{\otimes 3} \\ = & |0\rangle\langle 0| \otimes (|0\rangle\langle 0| + |1\rangle\langle 1|)^{\otimes 3} - |1\rangle\langle 1| \otimes (|0\rangle\langle 0| \\ & + |1\rangle\langle 1|)^{\otimes 3}, \end{aligned} \quad (\text{A3})$$

which can extract the diagonal information from the density matrix ρ_f of the final state after quench dynamics. The population of diagonal elements in ρ_f happens to the site-resolved particle density. Explicitly, $n_{\text{I},1} = a_1^* a_1$, $n_{\text{I},2} = a_2^* a_2, \dots, n_{\text{IV},3} = -a_{15}^* a_{15}$, $n_{\text{IV},4} = -a_{16}^* a_{16}$.

Here we take the measurement operation of $P_{|0001\rangle}$ as an example:

$$\begin{aligned} P_{|0001\rangle} = & |0\rangle\langle 0| \otimes |0\rangle\langle 0| \otimes |0\rangle\langle 0| \otimes |1\rangle\langle 1| \\ = & \frac{I_2 + \sigma_z}{2} \otimes \frac{I_2 + \sigma_z}{2} \otimes \frac{I_2 + \sigma_z}{2} \otimes \frac{I_2 - \sigma_z}{2} \\ = & (I_2 I_2 I_2 I_2 - I_2 I_2 I_2 \sigma_z + I_2 I_2 \sigma_z I_2 - I_2 I_2 \sigma_z \sigma_z + \\ & I_2 \sigma_z I_2 I_2 - I_2 \sigma_z I_2 \sigma_z + I_2 \sigma_z \sigma_z I_2 - I_2 \sigma_z \sigma_z \sigma_z + \\ & \sigma_z I_2 I_2 I_2 - \sigma_z I_2 I_2 \sigma_z + \sigma_z I_2 \sigma_z I_2 - \sigma_z I_2 \sigma_z \sigma_z + \\ & \sigma_z \sigma_z I_2 I_2 - \sigma_z \sigma_z I_2 \sigma_z + \sigma_z \sigma_z \sigma_z I_2 - \sigma_z \sigma_z \sigma_z \sigma_z) / 16. \end{aligned} \quad (\text{A4})$$

Only the x or y components of the first qubit can be read out directly in the NMR system of the $\text{C}_2\text{F}_3\text{I}$ molecule. For other z components, we can apply $\pi/2$ rotation pulse $R_{x,y}^{2,3,4}(\pi/2)$ on other qubits to make it along the x/y axis. Based on this, after multiple measurements, we can calculate the MCQM utilizing Eq. (A2) from the expectation value of $\langle \sigma_z \rangle$ of the first qubit (^{13}C).

[1] M. Cyrot, *Rep. Prog. Phys.* **36**, 103 (1973).

[2] J. M. Kosterlitz and D. J. Thouless, *J. Phys. C* **6**, 1181 (1973).

[3] K. v. Klitzing, G. Dorda, and M. Pepper, *Phys. Rev. Lett.* **45**, 494 (1980).

- [4] D. C. Tsui, H. L. Stormer, and A. C. Gossard, *Phys. Rev. Lett.* **48**, 1559 (1982).
- [5] X.-G. Wen, *Rev. Mod. Phys.* **89**, 041004 (2017).
- [6] X.-L. Qi and S.-C. Zhang, *Rev. Mod. Phys.* **83**, 1057 (2011).
- [7] M. Kohmoto, *Ann. Phys. (NY)* **160**, 343 (1985).
- [8] Q. Niu, D. J. Thouless, and Y.-S. Wu, *Phys. Rev. B* **31**, 3372 (1985).
- [9] M. D. Caio, N. R. Cooper, and M. J. Bhaseen, *Phys. Rev. Lett.* **115**, 236403 (2015).
- [10] L. D'Alessio and M. Rigol, *Nat. Commun.* **6**, 8336 (2015).
- [11] L. Zhang, L. Zhang, S. Niu, and X.-J. Liu, *Sci. Bull.* **63**, 1385 (2018).
- [12] L. Zhang, L. Zhang, and X.-J. Liu, *Phys. Rev. A* **99**, 053606 (2019).
- [13] C. Yang, L. Li, and S. Chen, *Phys. Rev. B* **97**, 060304(R) (2018).
- [14] C. Wang, P. Zhang, X. Chen, J. Yu, and H. Zhai, *Phys. Rev. Lett.* **118**, 185701 (2017).
- [15] M. Ezawa, *Phys. Rev. B* **98**, 205406 (2018).
- [16] M. Maffei, A. Dauphin, F. Cardano, M. Lewenstein, and P. Massignan, *New J. Phys.* **20**, 013023 (2018).
- [17] D. Xie, W. Gou, T. Xiao, B. Gadway, and B. Yan, *npj Quantum Inf.* **5**, 1 (2019).
- [18] W. P. Su, J. R. Schrieffer, and A. J. Heeger, *Phys. Rev. Lett.* **42**, 1698 (1979).
- [19] F. Liu and K. Wakabayashi, *Phys. Rev. Lett.* **118**, 076803 (2017).
- [20] C.-K. Chiu, J. C. Y. Teo, A. P. Schnyder, and S. Ryu, *Rev. Mod. Phys.* **88**, 035005 (2016).
- [21] T. Mizoguchi, Y. Kuno, and Y. Hatsugai, *Phys. Rev. Lett.* **126**, 016802 (2021).
- [22] G. Jotzu, M. Messer, R. Desbuquois, M. Lebrat, T. Uehlinger, D. Greif, and T. Esslinger, *Nature (London)* **515**, 237 (2014).
- [23] M. Leder, C. Grossert, L. Sitta, M. Genske, A. Rosch, and M. Weitz, *Nat. Commun.* **7**, 13112 (2016).
- [24] N. Goldman, J. C. Budich, and P. Zoller, *Nat. Phys.* **12**, 639 (2016).
- [25] E. Flurin, V. V. Ramasesh, S. Hacothen-Gourgy, L. S. Martin, N. Y. Yao, and I. Siddiqi, *Phys. Rev. X* **7**, 031023 (2017).
- [26] J. Niu, T. Yan, Y. Zhou, Z. Tao, X. Li, W. Liu, L. Zhang, H. Jia, S. Liu, Z. Yan, Y. Chen, and D. Yu, *Sci. Bull.* **66**, 1168 (2021).
- [27] F. Cardano, A. D'Errico, A. Dauphin, M. Maffei, B. Piccirillo, C. de Lisio, G. De Filippis, V. Cataudella, E. Santamato, L. Marrucci *et al.*, *Nat. Commun.* **8**, 15516 (2017).
- [28] E. J. Meier, F. A. An, A. Dauphin, M. Maffei, P. Massignan, T. L. Hughes, and B. Gadway, *Science* **362**, 929 (2018).
- [29] T. Xin, Y. Li, Y.-a. Fan, X. Zhu, Y. Zhang, X. Nie, J. Li, Q. Liu, and D. Lu, *Phys. Rev. Lett.* **125**, 090502 (2020).
- [30] A. D'Errico, F. Di Colandrea, R. Barboza, A. Dauphin, M. Lewenstein, P. Massignan, L. Marrucci, and F. Cardano, *Phys. Rev. Research* **2**, 023119 (2020).
- [31] D. G. Cory, A. F. Fahmy, and T. F. Havel, *Proc. Natl. Acad. Sci. USA* **94**, 1634 (1997).
- [32] W. S. Warren, N. Gershenfeld, and I. Chuang, *Science* **277**, 1688 (1997).
- [33] L. M. K. Vandersypen and I. L. Chuang, *Rev. Mod. Phys.* **76**, 1037 (2005).
- [34] T. Xin, B.-X. Wang, K.-R. Li, X.-Y. Kong, S.-J. Wei, T. Wang, D. Ruan, and G.-L. Long, *Chin. Phys. B* **27**, 020308 (2018).
- [35] M. Jiang, J. Bian, Q. Li, Z. Wu, H. Su, M. Xu, Y. Wang, X. Wang, and X. Peng, *Fundamental Research* **1**, 68 (2021).
- [36] W. A. Benalcazar, B. A. Bernevig, and T. L. Hughes, *Science* **357**, 61 (2017).
- [37] W. A. Benalcazar, B. A. Bernevig, and T. L. Hughes, *Phys. Rev. B* **96**, 245115 (2017).
- [38] J. Li, R. Fan, H. Wang, B. Ye, B. Zeng, H. Zhai, X. Peng, and J. Du, *Phys. Rev. X* **7**, 031011 (2017).
- [39] Z. Li, X. Liu, H. Wang, S. Ashhab, J. Cui, H. Chen, X. Peng, and J. Du, *Phys. Rev. Lett.* **122**, 090504 (2019).
- [40] H. Zhou, Y. Ji, X. Nie, X. Yang, X. Chen, J. Bian, and X. Peng, *Phys. Rev. Applied* **13**, 044059 (2020).
- [41] X. Nie, B.-B. Wei, X. Chen, Z. Zhang, X. Zhao, C. Qiu, Y. Tian, Y. Ji, T. Xin, D. Lu, and J. Li, *Phys. Rev. Lett.* **124**, 250601 (2020).
- [42] H. Wang, S. Wei, C. Zheng, X. Kong, J. Wen, X. Nie, J. Li, D. Lu, and T. Xin, *Phys. Rev. A* **102**, 012610 (2020).
- [43] J. Wen, C. Zheng, Z. Ye, T. Xin, and G. Long, *Phys. Rev. Research* **3**, 013256 (2021).
- [44] T. Xin, L. Che, C. Xi, A. Singh, X. Nie, J. Li, Y. Dong, and D. Lu, *Phys. Rev. Lett.* **126**, 110502 (2021).
- [45] X. Peng, X. Zhu, X. Fang, M. Feng, K. Gao, X. Yang, and M. Liu, *Chem. Phys. Lett.* **340**, 509 (2001).
- [46] T. Xin, L. Hao, S.-Y. Hou, G.-R. Feng, and G.-L. Long, *Sci. China: Phys. Mech. Astron.* **62**, 960312 (2019).
- [47] J. Wen, X. Qiu, X. Kong, X. Chen, F. Yang, and G. Long, *Sci. China: Phys. Mech. Astron.* **63**, 230321 (2020).
- [48] E. Knill, R. Laflamme, R. Martinez, and C.-H. Tseng, *Nature (London)* **404**, 368 (2000).
- [49] W. Sun, C.-R. Yi, B.-Z. Wang, W.-W. Zhang, B. C. Sanders, X.-T. Xu, Z.-Y. Wang, J. Schmiedmayer, Y. Deng, X.-J. Liu, S. Chen, and J.-W. Pan, *Phys. Rev. Lett.* **121**, 250403 (2018).
- [50] L. Zhang, L. Zhang, and X.-J. Liu, *Phys. Rev. A* **100**, 063624 (2019).
- [51] N. Khaneja, T. Reiss, C. Kehlet, T. Schulte-Herbrüggen, and S. J. Glaser, *J. Magn. Reson.* **172**, 296 (2005).
- [52] H.-J. Ding and R.-B. Wu, *Phys. Rev. A* **100**, 022302 (2019).
- [53] E. Knill, *Nature (London)* **434**, 39 (2005).
- [54] B.-X. Wang, T. Xin, X.-Y. Kong, S.-J. Wei, D. Ruan, and G.-L. Long, *Phys. Rev. A* **97**, 042345 (2018).
- [55] G. Long, G. Feng, and P. Sprenger, *Quantum Engineering* **1**, e27 (2019).
- [56] F. Schindler, A. M. Cook, M. G. Vergniory, Z. Wang, S. S. Parkin, B. A. Bernevig, and T. Neupert, *Sci. Adv.* **4**, eaat0346 (2018).
- [57] C. Wu, X. Guan, J. Fan, G. Chen, and S. Jia, *Phys. Rev. A* **104**, 022601 (2021).